Controlling the stimulated Brillouin scattering of self-focusing nanosecond laser pulses in silica glasses

Sarah Mauger,[1] Luc Bergé,[1] and Stefan Skupin[2,3]
[1]*CEA-DAM, DIF, F-91297 Arpajon, France*
[2]*Max Planck Institute for the Physics of Complex Systems, D-01187 Dresden, Germany*
[3]*Friedrich Schiller University, Institute of Condensed Matter Theory and Optics, D-07743 Jena, Germany*
(Received 25 January 2011; published 22 June 2011)

We numerically investigate the interplay between Kerr self-focusing (SF) and transient stimulated Brillouin scattering (SBS) for nanosecond pulses in bulk silica. The influences of the input power, phase, or amplitude modulations in the pump pulse together with the incident beam shape on the filamentation dynamics are discussed. We show that appropriate amplitude modulations dividing nanosecond laser pumps into picosecond-long pulse trains inhibit SBS at any power. In contrast, phase-modulated pulses with comparable spectral width undergo multiple filamentation and earlier beam collapse due to modulational instabilities. We demonstrate, however, the existence of a critical pump bandwidth above which SBS can be efficiently suppressed by phase modulations even at high powers. This observation also holds for squared beam shapes with much broader spatial spectra, which decay more easily into multiple filaments over short distances. Intensity profiles of the reflected Stokes waves for such broad pumps are finally discussed.

DOI: 10.1103/PhysRevA.83.063829 PACS number(s): 42.65.Es, 42.65.Jx, 42.70.Ce

I. INTRODUCTION

In nonlinear optics, stimulated Brillouin scattering (SBS) is a prominent process that occurs in various settings, such as optical fibers [1], nanostructured materials [2], or silica devices employed in high-power laser systems [3–6]. Because SBS generates frequency-shifted coherent light as well as phase conjugate waves, its application areas are numerous, from fiber-optical telecommunication technology to the development of tunable laser sources or Brillouin amplifiers and sensors. Moreover, SBS plays an important role in slow light propagation [7–9], light storing [10], and stimulated Rayleigh-Bragg scattering [11].

In the absence of optical absorption, SBS is excited by electrostriction of the bulk medium, which tends to become more dense in the regions of high fields through the increase of the local pressure. Nanosecond laser pulses can then excite an acoustic wave on which a Stokes wave scatters in the backward direction mainly [12,13]. The amplitude of this backward-propagating Stokes wave grows exponentially and can damage the front surface of the sample at sufficiently high input powers.

Since its first observation in the 60s, SBS has been extensively studied in many configurations applied to narrow or broadband pump lasers [14–20]. However, most of these works remained confined to one-dimensional (1D) geometries and they discarded the Kerr optical response of the material, apart from a few investigations limited to low pump intensities [21,22]. For many practical applications involving powerful pump pulses propagating in bulk $(3+1)$-dimensional geometries, however, the coupling between Kerr and SBS nonlinearities becomes highly relevant. In particular, for powers above the critical value for self-focusing (SF), the (forward) pump pulse can suffer severe modulational instabilities and even wave collapse [23]. These sharp dynamics are currently met in the optics of large-scale laser facilities devoted to inertial confinement fusion [24]. In this context, high-energy nanosecond pulses often initiate front damage in silica glasses due to SBS [4,6] and they moreover cause rear and bulk damages driven by Kerr filamentation [3]. Preventing laser-induced damage of dielectrics has thus become a challenging issue. For this purpose, exploiting multimode broadband pump pulses has been proposed to suppress at least SBS at infrared (1064 nm, 1ω) and ultraviolet (355 nm, 3ω) center wavelengths. Such multimode pumps are, however, reported to decrease substantially the SF distances, making filaments occur earlier inside the material at high power levels [3].

Therefore, the goal of this paper is to examine SBS efficiency in the presence of Kerr nonlinearities triggering either single or multiple filamentation, depending not only on the pump beam shape but also on specific input modulations currently used to weaken SBS. By means of fully space-time resolved (3D) simulations, we show that for powerful pumps a broad spectral bandwidth sustained by rapid phase modulations may not be efficient enough to avoid SBS-driven damages at the front surface of the propagation sample, whenever the modulation frequency lies below a critical value. In contrast, suitable amplitude modulations can drastically attenuate the stimulated scattering [25], at the expense of a halved average beam energy.

The paper is organized as follows. Section II recalls the model equations and their basic properties. Deviations to the propagation equations introduced by dispersion or plasma generation are discussed in the Appendix. Numerical results are presented in Sec. III. Whereas phase modulations with moderate bandwidths of $\sim$100 GHz can suppress SBS at low input powers, this property, however, no longer holds at high laser powers for which Kerr self-focusing comes into play. Only amplitude modulations creating ps-short pulse trains are found capable of eliminating backscattering, unless the pump spectral bandwidth supported by phase modulations with minimum number of modes exceeds a critical value. Finally, in Sec. IV, we investigate the multiple filamentation regime and how it develops depending on the initial pump beam shape.

II. MODEL EQUATIONS AND BASIC PROPERTIES

We first outline the set of equations describing the coupling between Brillouin and Kerr self-focusing effects. Basic properties of 1D SBS-active materials and multidimensional Kerr systems are then briefly reviewed.

A. Propagation equations

A linearly polarized forward pump pulse with nanosecond duration at center wavelength λ_0 is able to generate an acoustic wave via electrostriction through a few centimeters of bulk silica [12]. Part of the incident energy is then scattered back on this sound wave, creating a backward Stokes pulse. Our model equations describe this coupling between the two optical pump and Stokes waves and the acoustic wave. Two domains of optical wavelengths are investigated, namely, ultraviolet (UV, $\lambda_0 = 355$ nm) and infrared (IR, $\lambda_0 = 1064$ nm) wavelengths. Considering the two-component optical electric field

$$E = \sqrt{\frac{\omega_0\mu_0}{2k_0}}[U_1 e^{ik_0 z - i\omega_0 t} + U_2 e^{-ik_0 z - i\omega_0 t} + U_1^* e^{-ik_0 z + i\omega_0 t} + U_2^* e^{ik_0 z + i\omega_0 t}], \quad (1)$$

where μ_0 is the magnetic permeability in vacuum, the slowly varying envelopes of the forward and backward pulses, U_1 and U_2, respectively, have center frequencies $\omega_i \simeq \omega_0 = 2\pi c/\lambda_0\,(i = 1,2)$ and wave numbers $k_i \simeq n_0\omega_0/c = k_0$ in silica with linear index n_0 (c is the speed of light in vacuum). Governing equations for U_1 and U_2 are derived from the inhomogeneous Helmholtz equation

$$\vec{\nabla}^2 E - \frac{1}{c^2}\partial_t^2 E = \mu_0\left(\partial_t^2 P + \partial_t J\right), \quad (2)$$

where P is the polarization vector containing linear and nonlinear components, i.e.,

$$P = \epsilon_0\chi^{(1)}E + \epsilon_0\chi^{(3)}E^3 + \epsilon_0\Delta\epsilon E. \quad (3)$$

In Eq. (3), the first contribution refers to linear polarization with $\chi^{(1)}$ being the linear susceptibility. The second one describes the nonlinear optical polarization with the cubic susceptibility $\chi^{(3)}$. Note that we neglect both group-velocity dispersion (see Appendix A) and nonlinear dispersion; i.e., we assume $\chi^{(1)} \equiv \chi^{(1)}(\omega_0)$ and $\chi^{(3)} \equiv \chi^{(3)}(\omega_0,\omega_0,-\omega_0)$ in the relevant spectral range. The third contribution is the electrostriction polarization where $\Delta\epsilon = \gamma_e\Delta\rho/\rho_0$ represents variations in the dielectric constant, induced by acoustic density fluctuations $\Delta\rho$. Here, the coefficient of electrostriction γ_e is taken for a background material density ρ_0. Following Ref. [12], we assume that the density fluctuations obey the acoustic wave equation

$$\left[\partial_t^2 - \Gamma'\vec{\nabla}^2\partial_t - C_S^2\vec{\nabla}^2\right]\Delta\rho = \vec{\nabla}\cdot\vec{f}_e, \quad (4)$$

where Γ' is related to the phonon lifetime, $C_s = 5.97\times 10^5$ cm/s is the sound wave velocity, and $\vec{f}_e$ is the electrostrictive force. For our electric field, which propagates mainly in the z direction, this force is evaluated by

$$\vec{\nabla}\cdot\vec{f}_e = \frac{\gamma_e}{2n_0 c}q^2[U_1 U_2^* e^{i(qz-\Omega t)} + \text{c.c.}], \quad (5)$$

with $\vec{q} = \vec{k}_1 - \vec{k}_2$ and $\Omega = \omega_1 - \omega_2$ (c.c. means complex conjugate). Hence, we expect density fluctuations of the form

$$\Delta\rho = \bar{\rho}e^{i(qz-\Omega t)} + \text{c.c.}, \quad (6)$$

where $\bar{\rho}$ is the slowly varying envelope of the acoustic wave. J is the current density associated with plasma generation and the dynamic of charged particles (e.g., free electrons). Because linear dispersion is limited to first order, we can identify the group velocities of U_1 and U_2 as $k' \simeq k_0/\omega_0$. The phonon wave has the wave number $q \simeq 2k_1$ and frequency $\Omega \simeq \Omega_B = C_s q$. Equations for the slowly varying envelopes U_1, U_2, and $\bar{\rho}$ are derived from substituting Eq. (1) into Eq. (2) and Eq. (6) into Eq. (4), respectively, and omitting higher-order derivatives and phonon propagation. Moreover, in the expression for the polarization [Eq. (3)] we neglect harmonic generation and retain only self- and cross-phase modulations with Kerr nonlinear index $n_2 \equiv 3\mu_0 c\chi^{(3)}/4n_0^2$ [13,21]. Assuming moderate fluences $F_i \equiv \int |U_i|^2 dt < 12$ J/cm^2, we further discard plasma generation ($J \simeq 0$) responsible for damages in the material (see also Appendix B). The final equations describing the coupling between the Kerr nonlinearity and SBS can then be expressed as

$$(\partial_z + k'\partial_t)U_1 = \frac{i\vec{\nabla}_\perp^2 U_1}{2k_0} - \frac{g_0}{2}QU_2 + \frac{in_2\omega_0}{c}(|U_1|^2 + 2|U_2|^2)U_1, \quad (7)$$

$$(-\partial_z + k'\partial_t)U_2 = \frac{i\vec{\nabla}_\perp^2 U_2}{2k_0} + \frac{g_0}{2}Q^*U_1 + \frac{in_2\omega_0}{c}(|U_2|^2 + 2|U_1|^2)U_2, \quad (8)$$

$$\tau_B\partial_t Q + Q = U_1 U_2^* + N, \quad (9)$$

where z is the propagation variable, $\vec{\nabla}_\perp^2 = \partial_x^2 + \partial_y^2$ is the diffraction operator, $Q \equiv 2\Gamma_B n_0 c C_S\bar{\rho}/iq\gamma_e$ denotes the scaled density fluctuation envelope, $\tau_B = 2/\Gamma_B = 2/q^2\Gamma'$ is the phonon damping rate, and $g_0 = \omega_0^2 n_0^7 p_{12}^2/C_S c^3\rho_0\Gamma_B \simeq 4.5$ cm/GW is the gain factor computed from the bulk density $\rho_0 = 2.21$ g/cm^3 and the elasto-optic coefficient p_{12} [1,13,21]. Γ_B is the Brillouin linewidth related to the full-width at half-maximum of the Brillouin gain spectrum as $\Delta\nu_B = \Gamma_B/2\pi$ and it varies like $1/\lambda_0^2$. According to Refs. [1,21], the value of p_{12} ranges between 0.27 and 0.286 for laser wavelengths included in the interval $355 \leqslant \lambda_0 \leqslant 1064$ nm. Thus, g_0 does not vary so much with λ_0, i.e., $4.4 \leqslant g_0 \leqslant 5.2$ cm/GW [4]. Fixing $p_{12} = 0.27$, this gives an uncertainty on the self-focusing distances limited to 10% over all laser wavelengths, which we ignore in the coming analysis. Numerical values for the other relevant physical parameters are given in Table I, for both UV and IR wavelengths. The field envelopes U_i have been normalized such that $I_i = |U_i|^2$ is their intensities expressed in W/cm^2. The phonon damping length, C_s/Γ_B, is limited to a few tens of micrometers, which allows us to discard the spatial

TABLE I. Physical parameters for silica at 355 and 1064 nm.

Physical parameters	$\lambda_0 = 355$ nm	$\lambda_0 = 1064$ nm
n_0	1.4762	1.454
P_{cr} (MW)	0.35	4.27
n_2 (cm^2/W)	3.6×10^{-16}	2.7×10^{-16}
ω_0 (fs^{-1})	5.31	1.77
τ_B (ns)	1.1	10

dynamics of the acoustic wave envelope. In Eq. (9), N models a thermally driven Gaussian random noise that initiates SBS, with zero mean $\langle N(\vec{r},t)\rangle = 0$ and

$$\langle N(\vec{r},t)N^*(\vec{r}',t')\rangle = A_N\delta(\vec{r}-\vec{r}')\delta(t-t'), \tag{10}$$

where $A_N = (2n_0c/q\gamma_e)^2(2k_BT\rho_0\Gamma_B)$ depends on $\gamma_e \simeq n_0^4 p_{12} \approx 1.6$, the bulk temperature $T = 300$ K, and Boltzmann constant k_B [17]. In the following, Eqs. (7)–(9) are numerically integrated in full 3D geometry, first for an input pump with spatial and temporal Gaussian profiles

$$U_1(z=0) = \sqrt{I_1(0)}\exp\left[-(x^2+y^2)/w_0^2 - t^2/t_p^2\right], \tag{11}$$

initial waist $w_0 = 150$ μm, and $1/e^2$ duration $t_p = 2.12$ ns (Sec. III), and then for supergaussian spatial profiles (Sec. IV C). The silica sample thickness is either $L = 5$ cm or $L = 10$ cm. Because SBS is a source of damage at the front surface of the sample, pump pulses with appropriate phase or amplitude modulations will be examined in order to limit backscattering. We use a split-step parallel spectral code running over 128 processors with the longitudinal grid spacing $\Delta z = \Delta t/k'$, down to 12 μm, where $k' = n_0/c$ and Δt is the time step. Spatial resolutions in the transverse diffraction plane are $\Delta x = \Delta y = 3.9$ μm.

B. Basic behaviors

Equations (7)–(9) describe the interplay between SF and SBS. The typical length scales for diffraction, $L_{\rm diff} = 2k_0w_0^2$, self-focusing, $L_{\rm SF} = c/\omega_0 n_2 I_1(0)$, and SBS, $L_B = 1/g_0 I_1(0)$, obey the inequality $L_B < L_{\rm SF} \ll L_{\rm diff}$ for pump intensities above 5 GW/cm^2.

Because the product $\Gamma_B t_p$ is of order unity, SBS develops in a transient regime, for which the 1D gain [no (x,y) dependency of the fields], assuming the large gain limit, is classically evaluated in the undepleted pump approximation [15,19] by

$$\frac{U_2(z,t)}{U_2(L,t)} \propto \int_{-\infty}^{t} e^{-\frac{\Gamma_B}{2}(t-t')+\sqrt{g_0\Gamma_B(L-z)\int_{t'}^{t}|U_1(\eta)|^2 d\eta}} \times U_1(z,t)U_1^*(z,t')dt'. \tag{12}$$

For a plane-wave pump, the nonstationary intensity gain is mainly given by $G_T \sim 2\sqrt{\Gamma_B t_p(L-z)/L_B}$. In the stationary limit reached when $\Gamma_B t_p \to +\infty$, the classical stationary gain $G_S = (L-z)/L_B$ is recovered by maximizing the exponential argument of Eq. (12).

Besides, the Kerr response, although originally weak ($\omega_0 n_2/g_0 c < 2 \times 10^{-2}$), is expected to cause wave collapse at high powers $P_i \equiv \int I_i d\vec{r}_\perp$ [26]. For negligible SBS ($g_0 \to 0$), the mean-square radius integrals of the two counterpropagating pump and Stokes components evolve along the z axis as $d_z^2 \int r_\perp^2 (I_1 + I_2) d\vec{r}_\perp = 4H_{\rm SF}/k_0$, where $H_{\rm SF}$ denotes the Hamiltonian for self-focusing

$$H_{\rm SF} = \sum_{i=1,2}\int\left[\frac{|\vec{\nabla}_\perp U_i|^2}{2k_0} - \frac{n_2\omega_0}{2c}\left(I_i^2 + 4I_1I_2\right)\right]d\vec{r}_\perp. \tag{13}$$

By applying Schwarz and Sobolev inequalities [26], forward (pump) blowup is found to require an input power satisfying $P_1(0) \geqslant P_{\rm cr}/(1+2R)$, where $R \equiv P_2(0)/P_1(0)$ and $P_{\rm cr} \equiv 3.72\lambda_0^2/(8\pi n_0 n_2)$ is the usual critical power for self-focusing. In the limit $P_2(0) \to 0$, the SF threshold for a single wave is retrieved. Note that we neglect here any power exchange between the forward and backward waves ($g_0 \to 0$), which leads to a decrease of the effective blowup power threshold. When the backward wave is created via SBS, we expect a delayed self-focusing dynamics (increase of blowup threshold) for the forward pump due to energy depletion. In the pure forward case [$P_2(0) \to 0$] and for an unperturbed Gaussian beam, the collapse distance can be estimated by Marburger's formula [27]

$$z_c \simeq L_M = \frac{0.092L_{\rm diff}}{[(\sqrt{P_1(0)/P_{\rm cr}} - 0.852)^2 - 0.0219]^{1/2}}. \tag{14}$$

Pump pulses containing many critical powers can instead decay into multiple filaments seeded by modulational instability [28]. In that case, beam collapse takes place at earlier distances,

$$z_c \simeq L_{\rm SF} = \lambda_0/2\pi n_2 I_1(0), \tag{15}$$

yielding a direct dependence on the initial pump power $z_c \sim 1/P_1(0)$ [29,30]. In Eq. (15), the right-hand side is nothing else but the inverse of the maximum growth rate $\gamma_1 = n_2\omega_0 I_1(0)/c$ of oscillatory perturbations acting on a single plane-wave pump. The filamentation behavior, single or multiple, also depends on the initial beam-shape [31]. For example, for high-order supergaussian profiles, multiple filamentation is promoted on the edges of the beam, whereas Gaussian beams undergo single filamentation at moderate peak powers.

III. SINGLE FILAMENTATION OF THE PUMP

We now determine the power threshold from which a single filament can emerge from the coupling between SBS and Kerr effects affecting a Gaussian pump beam. Different modulations are then applied to the incident pulse in order to weaken SBS. In the following two subsections, characteristic behaviors reported in Ref. [25] are briefly recalled.

A. Low powers

We begin with low input powers $P_1(0) < 14P_{\rm cr}$ leading to slow self-focusing inside a silica sample with thickness $L = 5$ cm. Figures 1(a) and 1(b) show the maximum intensities and partial energies $E_i(z) \equiv \int F_i d\vec{r}_\perp$ of the pump and Stokes waves for an unmodulated pump pulse with power $P_1(0) = 5P_{\rm cr}$. We carefully checked that the conservation law $E_1(z) - E_2(z) = $ const. was fulfilled in all our numerical simulations. We observe in Fig. 1(a) that, without any modulation, the pump intensity slowly increases due to self-focusing and a Stokes wave is generated inside the 5-cm-thick sample via

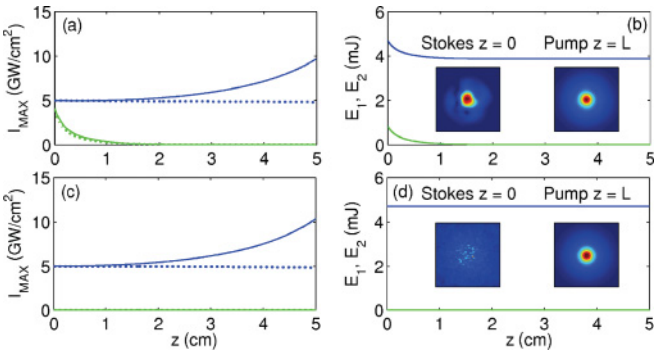

FIG. 1. (Color online) Peak intensities [(a), (c)] and partial energies [(b),(d)] for 355-nm Gaussian input pulses with $w_0 = 150\ \mu$m, $t_p = 2.12$ ns, and $P_1(0) = 5P_{\rm cr}$. Top figures refer to an unmodulated beam and bottom ones show the case of a phase-modulated beam for which $m = 21$ and $\nu_m = 2$ GHz. Blue (dark gray) curves refer to the pump pulse and green (light gray) curves represent the Stokes pulse. Solid lines correspond to the complete Eqs. (7)–(9) whereas dotted lines discard the full Kerr response. Insets detail Stokes and pump fluence distributions in a $400 \times 400\ \mu$m^2 section of the (x,y) plane at $z = 0$ and $z = L = 5$ cm, respectively.

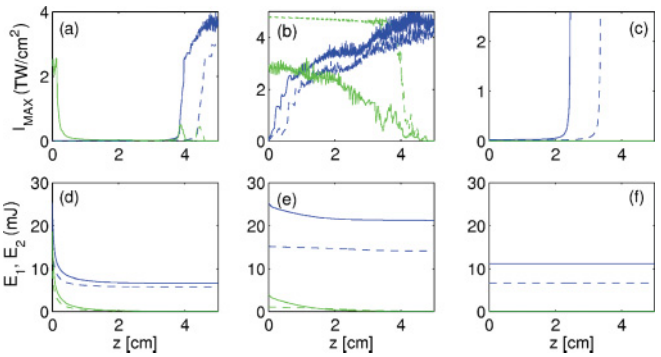

FIG. 2. (Color online) Peak intensities for 355-nm (a) unmodulated, (b) phase-modulated, and (c) amplitude-modulated input Gaussian pulses with $w_0 = 150\,\mu$m, $t_p = 2.12$ ns, $P_1(0) = 16P_{\rm cr}$ (dashed curves), and $P_1(0) = 27P_{\rm cr}$ (solid curves). Blue (dark gray) curves refer to the pump pulse and green (light gray) curves represent the Stokes pulse. Corresponding partial energies for (d) unmodulated, (e) phase-modulated, and (f) amplitude-modulated pump pulses.

SBS. This effect also clearly manifests in Fig. 1(b), where the partial energy of the pump is transferred to the Stokes wave.

SBS may be inhibited by phase modulations of the pump. It is indeed well-known [18,32] that multimode pumps with broad bandwidths $\Delta\nu$ trigger weaker Brillouin-reflected fluences. Assuring a small enough coherence length, $n_0\Delta\nu L_B/c \gg 1$, guarantees that the Stokes modes evolve independently of each other and only interact with their corresponding pump mode [33]. For this purpose, introducing a phase modulation $U_1 \to M(t) \times U_1$ with $M(t) = \exp[im\sin(2\pi\nu_m t)]$ creates a multimode spectrum of $1/e$ bandwidth $\Delta\nu \simeq 2m\nu_m$ (see Fig. 13 in Appendix A), where $2m$ is approximately the number of modes and ν_m the modulation frequency. We used a modulation depth $m = 21$ and frequency $\nu_m = 2$ GHz, providing a mode spacing larger than the Brillouin gain spectrum to prevent acoustic field enhancement by the neighboring pulse lines. The overall spectral bandwidth satisfying $\Delta\nu \gg \Delta\nu_B$ should result in the net decrease of the SBS gain. Since $\exp[im\sin(2\pi\nu_m t)] = \sum_{l=-\infty}^{l=+\infty} J_l(m)e^{2i\pi l\nu_m t}$, where $J_l(x)$ is the lth-order Bessel function $[\sum_l J_l^2(m) = 1]$, such phase modulation is expected [according to Eq. (12)] to decrease the SBS growth rate as $I_2(z,t)/I_2(L,t) \sim I_1(0)\sum_l J_l^2(m)\exp[L_B^{-1}(L-z)/(1+16\pi^2 l^2\nu_m^2/\Gamma_B^2)]$ at maximum gain in the plane-wave approximation. Indeed, when a phase modulation is applied to the incident pulse [Figs. 1(c) and 1(d)], the pump intensity still slowly increases via Kerr self-focusing but the Stokes intensity stays to zero, which is confirmed by the constant partial energies. The pump maximum intensity even increases to higher level because of the absence of SBS depletion. As evidenced by the dotted curves corresponding to numerical simulations discarding self- and cross-phase modulation terms, the Kerr response always increases the peak intensity of the two components in the sample.

B. High powers

At larger powers $14P_{\rm cr} < P_1(0) < 27P_{\rm cr}$, the pump collapses inside the 5-cm-long sample [Fig. 2(a)]. The self-focus point z_c of the pump clearly lies beyond that corresponding to the pure collapse of a single Gaussian wave ($L_{\rm M} \leqslant 3.4$ cm). At the front and rear surfaces, reflected Stokes and transmitted pump pulses can attain comparable intensities above the TW/cm^2 level, respectively. The Kerr response amplifies the two components near the pump focus z_c in the sample. Cross-phase modulation terms ($\sim n_2 I_i U_j$, with $i \neq j$) were observed to influence the growth of the Stokes intensity and participate in the SF process in the vicinity of this focus. Despite the important contribution of the Kerr nonlinearities, the pump nonlinear focus remains at comparable distances, $z_c \simeq 4$–4.5 cm, due to the pump depletion that significantly decreases the pump power in the early stage of propagation. In Fig. 2(d), we indeed see that the pump energy is rapidly depleted to the benefit of the Stokes component in the ratio $E_1(z_c)/E_1(0) \simeq 1/3$–$1/4$ for increasing powers. Inspection of the numerical data reveals that the Stokes fluence can approach the damage threshold $[F_2^{\max}(0) \simeq 11.4$ J/cm$^2]$, which suggests to employ pulse shaping techniques breaking the laser coherence to decrease this backward fluence.

However, it turns out that phase modulation is less efficient for high power pulses triggering SF, as evidenced in Fig. 2(b) where the Stokes wave sharply increases. The reason is that inhibiting SBS through phase modulation leads also to a much weaker pump depletion, $E_1(L)/E_1(0) \simeq 0.88$, over the sample thickness due to the reduced SBS gain [Fig. 2(e)]. Consequently, the pump gets stronger focused by the Kerr nonlinearities and self-focuses at shorter propagation distances. The reflected fluence is reduced, but it may still attain significant levels $\sim$7 J/cm^2 [25].

In contrast, nonperturbative amplitude modulations, using $M(t) = \cos[m\sin(2\pi\nu_m t)]$ with the same values of m and ν_m, keep the reflected Stokes intensity and energy close to zero, as shown by Figs. 2(c) and 2(f). Backscattering is suppressed and the pump wave undergoes SF at Marburger distance. The main reason for this behavior is the following: Mathematically,

$U_1(z,t)$ in Eq. (12) has an autocorrelation function equal to $\frac{I_1(0)}{2}\sum_{2k} J_{2k}^2(m)\cos[4k\pi\nu_m(t-t')]$, averaging all orders in the integral to zero. Physically, these modulations break the pump into pulse trains of short periods $1/m\nu_m \sim 24$ ps, which prevents the creation of acoustic matter waves. The resulting dynamic of the pump pulse is a wave collapse in the sense of a blowup singularity, as shown by Fig. 2(c). In this case, the solution for the pump U_1 does no longer exist for $z > z_c$. Of course, in real-world experiments, plasma generation due to medium ionization or higher-order nonlinearities would eventually kick in and stop the collapse.

In a more detailed analysis we numerically identified a threshold frequency, $\omega_{\rm cr} \simeq 0.8$ ns^{-1}, below which the amplitude modulations do not suppress SBS anymore. This threshold frequency corresponds to modulation periods approaching the phonon damping rate τ_B. Similar results hold for simpler modulations, i.e., $M(t) = |\cos(2m\pi\nu_m t)|$ or $M(t) = \cos^2(2m\pi\nu_m t)$. The price to pay for the previous technique is, however, that the average energy and power available in the overall modulated pulse (for fixed peak intensity) are divided by a factor close to 2. Indeed, we can evaluate the mean value of the beam power over $k \gg 1$ optical periods as

$$P_{\rm averaged} = \frac{\omega_0 P_1(0)}{2k\pi}\int_0^{2k\pi/\omega_0} M^2(t)e^{-2t^2/t_p^2}dt. \qquad (16)$$

Equation (16) reduces to $P_1(0)/f$ with a factor f varying between 2.6 and 3.2 following the amplitude functions.

Figure 3 shows the intensity profiles of unperturbed, phase- and amplitude-modulated pumps in the (z,t) plane and the corresponding Stokes profiles for $P_1(0) = 16P_{\rm cr}$. Close to the nonlinear focus, with no phase modulation, the pump front

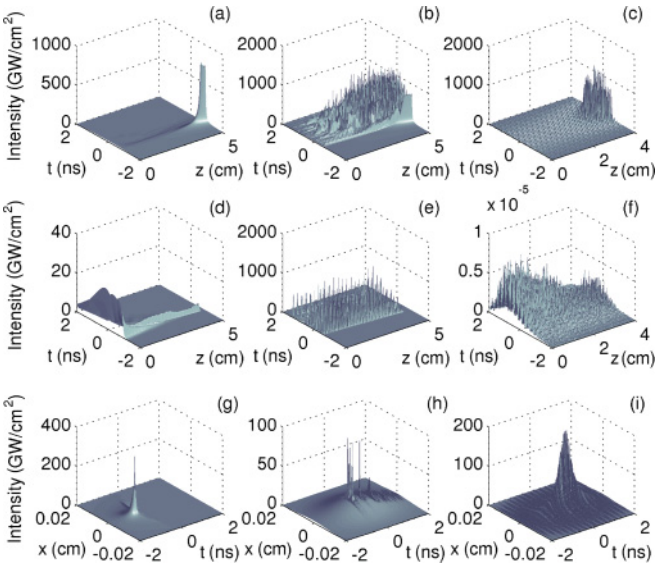

FIG. 3. (Color online) Intensity profiles in the (z,t) plane with maximum intensity for $P_1(0) = 16P_{\rm cr}$: without any modulation, (a) $I_{1\max}(z)$ and (d) $I_{2\max}(z)$; with a phase modulation, (b) $I_{1\max}(z)$ and (e) $I_{2\max}(z)$; with an amplitude modulation, (c) $I_{1\max}(z)$ and (f) $I_{2\max}(z)$ (note the factor 10^{-5} in the intensity scale). (g,h,i) Corresponding spatial profiles of the pump in the (x,t) plane near the collapse distance $z_c = 4.4$ cm without modulation, $z_c = 0.6$ cm with a phase modulation, and $z_c = 3.4$ cm with an amplitude modulation.

is depleted near the instant $t \simeq -1$ ns, from which a sharp Stokes spike emerges, grows at decreasing z while it covers the remaining pump extent in time. A singly peaked structure is amplified in the pump ($z_c \simeq 4.35$ cm) and in the Stokes pulses [Figs. 3(a), 3(d), and 3(g)]. In the case of a phase modulation, both forward and backward optical components break up into multiple peaks first in time, with forced periodicity $\approx 1/\nu_m$, and then in space through space-time couplings, as shown by Figs. 3(b), 3(e), and 3(h). Modulational instabilities are amplified, which drastically affects the filamentation dynamics (see Sec. IV A). In contrast, with an amplitude modulation, acoustic waves have no time to form, so that SBS is almost completely suppressed [Figs. 3(f) and 3(i)]. The maximum backscattered intensity remains negligible while the pump envelope is preserved. These behaviors are generic for the whole range of incident powers studied here.

At $\lambda_0 = 1064$ nm, the numerical data display the same dynamics for unmodulated pumps, whose depletion again takes place around $t \simeq -1$ ns, as well as for both phase and amplitude modulations. A noticeable difference lies in the intensity threshold $I_{\rm th}$ for the raising of a backward component, which is higher than for UV beams, namely, $I_{\rm th} \approx 35$ GW/cm^2 at IR wavelength, whereas $I_{\rm th} \approx 13$ GW/cm^2 at UV wavelength. The power threshold $P_{\rm th}$ necessary to reach the collapse regime also changes: $P_{\rm th} = 13P_{\rm cr} = 4.9$ MW for the UV wavelength whereas $P_{\rm th} = 3P_{\rm cr} = 12.8$ MW in the infrared domain. These differences can be attributed to the fact that the Kerr factor $n_2\omega_0/c$ and the Brillouin linewidth $\Gamma_B = 2/\tau_B$ are smaller for $\lambda_0 = 1064$ nm (see Table I). With moderate bandwidths $\leqslant$100 GHz, turbulent dynamics comparable with Figs. 3(b), 3(e), and 3(h) develop, and they vanish, as well as the Stokes wave, when amplitude modulations are applied.

C. Critical frequency for phase modulations

We have seen that phase modulations with bandwidth $\leqslant$100 GHz appear barely efficient to suppress SBS at high pump power. However, we may wonder whether there exists a critical bandwidth, depending on the initial intensity, above which phase modulations recover efficiency to inhibit SBS. Discarding the Gaussian noise N for simplicity, let us consider the equation for the rescaled density envelope Q [Eq. (9)]. Defining the phonon power by $W = \int |Q|^2 d\vec{r}_\perp$, one finds

$$\partial_t W + \Gamma_B W = \frac{\Gamma_B}{g_0}(-\partial_z + k'\partial_t)P_2 = -\frac{\Gamma_B}{g_0}(\partial_z + k'\partial_t)P_1, \qquad (17)$$

which can be integrated in time to yield

$$d_z E_1 = d_z E_2 = -g_0 \int\int_{-\infty}^{+\infty} |\widehat{Q}(\omega)|^2 d\omega d\vec{r}_\perp \qquad (18)$$

with Parseval-Plancherel theorem and zero boundary conditions. Here, the phonon density is expressed in the Fourier domain (symbol $\widehat{\ }$) as

$$|\widehat{Q}(\omega)|^2 = \left(\frac{\Gamma_B}{2}\right)^2 \frac{|\widehat{U_1 U_2^*}|^2}{\omega^2 + (\Gamma_B/2)^2}. \qquad (19)$$

According to Ref. [15], with the relative phases of U_1 and U_2 being random, $\widehat{U_1 U_2^*} \equiv \frac{1}{\sqrt{2\pi}} \int U_1(z,\vec{r}_\perp,t) U_2^*(z,\vec{r}_\perp,t) e^{i\omega t} dt$ gives

$$|\widehat{U_1 U_2^*}|^2 \simeq \frac{1}{\Delta\omega} \langle I_1(z,r_\perp,t)\rangle \int I_2 dt = \frac{\langle I_1\rangle}{\Delta\omega} F_2. \quad (20)$$

Here, $\langle I_1\rangle$ is the time average of the pump intensity with spectral width $\Delta\omega \equiv 2\pi\Delta\nu$. We thus find that the evolution of the Stokes energy is given by

$$-d_z E_2 = \frac{g_0 \pi \Gamma_B}{2\Delta\omega} \int d\vec{r}_\perp \langle I_1\rangle F_2. \quad (21)$$

Assuming $\frac{\pi w_0^2}{2} F_2 \simeq E_2$ and $\int d\vec{r}_\perp \langle I_1\rangle \simeq P_1(0)$, we obtain

$$E_2(z) \sim E_2(L) e^{\frac{g_0\Gamma_B}{\Delta\omega w_0^2} P_1(0)(L-z)}. \quad (22)$$

Limiting the growth of the Stokes energy then demands

$$\Delta\nu \gg \Delta\nu_{\rm cr} = \tfrac{1}{4}\Gamma_B g_0 I_1(0) L, \quad (23)$$

yielding a minimum value of the pump spectral bandwidth necessary to arrest SBS, as a function of the incident pump intensity.

Simulations have been performed to check the validity of Eq. (23). Figure 4(a) shows results for the numerically evaluated critical value of $\Delta\nu$ (solid curves) and for a slightly lower value (dashed curves) at two incident powers: in red (light gray), $P_1(0) = 49P_{\rm cr}$, and in blue (dark gray), $P_1(0) = 16P_{\rm cr}$. If the bandwidth is below critical, self-focusing occurs at a smaller distance along the optical path and the pump power profile is perturbed with periodic peaks corresponding to the modulation frequency (not shown). The Stokes component can then reach intensities higher than 100 GW/cm^2. In contrast, if a broad enough bandwidth is applied, the pump intensity purely collapses at Marburger distance with an aborted Stokes component. The inset shows that the Stokes intensity then reaches the MW/cm^2 range only and becomes meaningless. In Fig. 4(b), the value of the critical bandwidth estimated from our numerical simulations is given as a function of the initial intensity for a 5-cm-long sample. Results are also shown for a 10-cm-thick glass. Since SBS becomes more efficient over longer propagation lengths, the critical bandwidth becomes larger in turn. Almost all numerical results for the values of $\Delta\nu_{\rm cr}$ are found superior to the analytical evaluation given by Eq. (23). Although rough, this evaluation seems to provide a reliable lower bound for the numerically evaluated value of the critical bandwidth. Note that this value varies with the wavelength via Γ_B and should thus be smaller in the IR domain. This is actually confirmed: For example, with $I_1(0) \approx 38$ GW/cm^2, we find a critical bandwidth of $\simeq$ 730 GHz at IR wavelength, while $\Delta\nu_{\rm cr} \simeq 970$ GHz is requested in the UV domain.

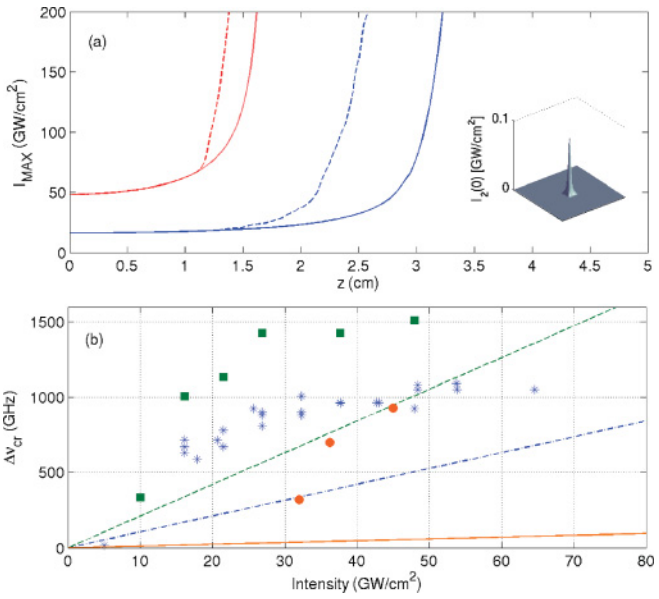

FIG. 4. (Color online) (a) Maximum pump intensity along z for $P_1(0) = 49P_{\rm cr}$ [red (light gray) curve] and $P_1(0) = 16P_{\rm cr}$ [blue (dark gray) curve]. The solid curves correspond to $\Delta\nu = \Delta\nu_{\rm cr}$, whereas the dashed curves represent the pump intensity with the same modulation frequency lowered by 1 GHz. The inset shows the Stokes intensity profile at $z = 0$ for $P_1(0) = 49P_{\rm cr}$ at the critical bandwidth. (b) Mapping of $\Delta\nu_{\rm cr}$ as a function of the initial pump intensity. Blue stars (green squares) correspond to $\lambda_0 = 355$ nm with $L = 5$ cm (respectively, $L = 10$ cm). Orange circles refer to data for $\lambda_0 = 1064$ nm in a 5-cm-long sample. Blue dash-dotted (green dashed) curves report the lower bound of Eq. (23) with $\lambda_0 = 355$ nm for $L = 5$ cm (respectively, $L = 10$ cm). The orange solid curve corresponds to the IR wavelength in a 5 cm-long sample.

Importantly, ensuring $\Delta\nu$ greater than $\Delta\nu_{\rm cr}$ is not sufficient because also a large number of modes is necessary to make phase modulation efficient. For example, numerous simulations have been made where, for low values of m, increasing $\Delta\nu$ only via the value of the modulation frequency ν_m could not reduce the Brillouin gain. On the basis of Refs. [4,12], an SBS generator medium, where stimulated scattering is initiated by noise, is expected to produce a Stokes signal if the exponential gain reaches a threshold $G_{\rm TH}$ which is, for most of materials, of the order of 25–30 (see also Refs. [34,35] for long optical fibers). In a nonstationary regime and assuming that the pump intensity is equally distributed on the $2m$ modes [33], the Brillouin gain should thus obey the condition $G_T = 2\sqrt{\Gamma_B t_p L/L_B} < G_{\rm TH}\sqrt{2m}$, or

$$m > m_{\rm cr} = G_T^2/2G_{\rm TH}^2, \quad (24)$$

providing minimum values of the modulation depth $m_{\rm cr} \approx 5$ to 10 for $G_{\rm TH} = 25$ and 30, respectively. These evaluations are found in reasonable agreement with our numerical estimates for $m_{\rm cr}$, i.e., $m_{\rm cr} = 6$ for $16P_{\rm cr} \leqslant P_1(0) \leqslant 27P_{\rm cr}$ and $m_{\rm cr} = 8$ for $38P_{\rm cr} \leqslant P_1(0) \leqslant 49P_{\rm cr}$. Note that the two criterions, Eqs. (23) and (24), do not depend on the Kerr parameters.

D. Summary using the breakup integral *B*

Gathering all the previous dynamics, Fig. 5 shows the so-called "breakup integral"

$$B = \frac{2\pi n_2}{\lambda_0} I_1(0) z_c, \quad (25)$$

which is proportional to the product of the initial pump intensity and self-focusing distance. The B integral is independent of the waist and of the wavelength, which offers a very convenient way to superimpose our numerical results

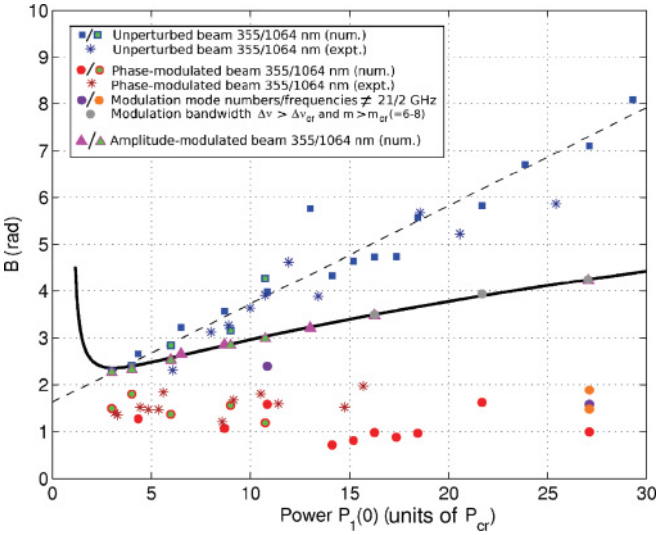

FIG. 5. (Color online) Mapping of the break-up integral B as a function of the initial pump power in terms of $P_{\rm cr}$. The black curve refers to Marburger's formula [27]. Blue squares correspond to data points for unmodulated beams; triangles report results from amplitude-modulated pumps. Below, red circles correspond to phase-modulated pumps with $m = 21$ and $\nu_m = 2$ GHz. Single color symbols refer to ultraviolet ($\lambda_0 = 355$ nm) wavelengths; symbols with green interior mark numerical results in the infrared ($\lambda_0 = 1064$ nm). Orange and violet circles refer to phase modulations with different number of modes ($m = 10$ or 42) and frequency ($\nu_m = 14$ GHz), respectively. Gray circles stand for phase-modulated cases with $\Delta\nu > \Delta\nu_{\rm cr}$. The star symbols recall experimental data for both wavelengths (see Ref. [3]). The dashed curve represents the straight line discussed in the text.

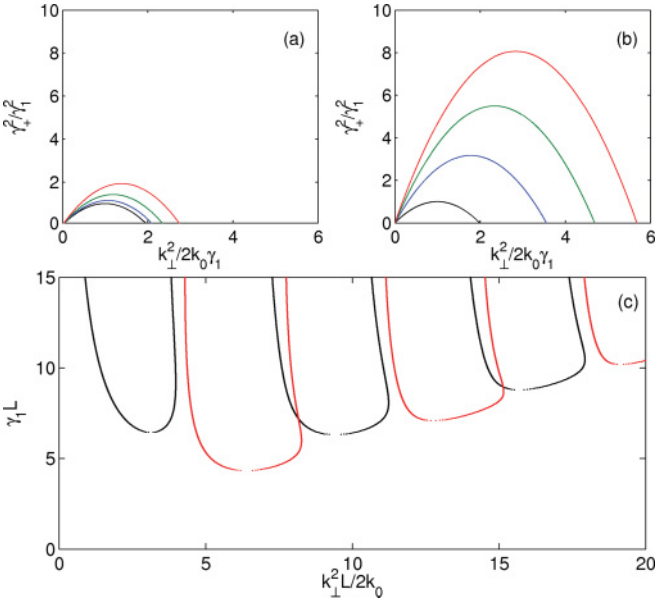

FIG. 6. (Color online) Normalized growth rate as a function of transverse wave number for different values of R_S with (a) $g_0 = 0.25$ cm/GW and (b) $g_0 = 0.1$ cm/GW. The black (lower) curve corresponds to the transverse modulational instability for a single pump wave and the red (upper) curve shows the transverse modulational instability of two equal counterpropagating waves. Blue and green (middle) curves represent calculations for $R_S = 0.33$ and $R_S = 0.67$, respectively. Panel (c) shows the normalized instability threshold intensity $\gamma_1 L$ satisfying Eq. (31) in a finite medium for $R_S = 10^{-3}$. The black curve corresponds to the case discarding SBS ($g_0 = 0$) whereas the red (gray) curve represents the case with a reduced Brillouin gain $g_0 = 4.5/\sqrt{2m} \approx 0.7$ cm/GW.

at different laser wavelengths. Here we have plotted data computed from additional numerics performed at 1064 nm. We also recall experimental data reported in Ref. [3]. For $P_1(0) \leqslant 4.2$ MW $= 12P_{\rm cr}$ at $\lambda_0 = 355$ nm and $P_1(0) \leqslant 12.8$ MW $= 3P_{\rm cr}$ at $\lambda_0 = 1064$ nm, simulations were performed using a smaller beam waist, in order to trigger a wave collapse inside the 5-cm glass thickness. The collapse distance is identified as the longitudinal location of the first pump peak widely exceeding $20 \times I_1(0)$.

With SBS, SF produces a nonlinear focus that does not significantly vary with the pump power: SF distances follow the empirical straight line $z_c = aw_0^2 + b/I_1(0)$ with $a \simeq 14.75 \times 10^3$ cm^{-1} and $b = 25.5$ GW/cm (dashed line). In contrast, when the pump is modulated in phase with a moderate bandwidth ~100 GHz, the breakup integral B saturates around 1.5 rad. This behavior agrees quite well with Fig. 6 of Ref. [3] and can be explained by the pulse spatiotemporal breakup undergone by the multimode pump [25]. Recalled by Eq. (15), the SF distances should then fulfill the relationship

$$z_c \simeq L_{\rm SF} \times E_1(0)/E_1(L), \tag{26}$$

where we included the partial energy ratio $E_1(0)/E_1(L)$, which reflects pump power depletion according to the power scaling of Ref. [30]. This relation indeed yields $B \simeq 1.4$ rad. On the contrary, when we apply a phase modulation with bandwidth over critical, the self-focusing distance is equal to the Marburger distance. Corresponding results are represented by gray circles on the Marburger (black) curve. Pink triangles on the same curve refer to amplitude-modulated pumps, for which SBS is also suppressed. Orange and violet circles refer to phase modulations with different values of the number of modes ($m = 10$ and $m = 42$) and of the modulation frequency ($\nu_m = 14$ GHz), respectively, which demonstrates the generic nature of our findings.

IV. MULTIPLE FILAMENTATION AND INFLUENCE OF THE BEAM SHAPE

This section is dedicated to the multiple filamentation regime. Phase modulations can trigger modulational instability, leading to temporal and spatial breakups of both pump and Stokes waves, which is investigated first. Next, the influence of the beam shape on the breakup is studied, using supergaussian profiles.

A. Modulational instabilities

Phase modulations of the pump reduce the effective Brillouin gain to the benefit of the Kerr nonlinearities. To explain this feature, we recall that in optical fibers the pump and Stokes envelopes undergoing rapid phase modulations become multimode, i.e., $U_i = \sum_n A_{i,n} e^{i(k_{i,n}z - \omega_{i,n}t)}$ ($i = 1,2$) with nonzero group-velocity mismatch. Assuring

small coherence length compared to L_B makes the pump and Stokes total intensities evolve according to $\partial_z I_i \sim -\bar{\gamma} g_0 I_i I_j$ $(i \neq j)$ in the stationary limit. Here, $I_i = \sum_{n=1}^{2m} |A_{i,n}|^2$ and $\bar{\gamma} = \sum_{n=1}^{2m} |A_{1,n} A_{2,n}|^2 / I_1 I_2$ divides the SBS gain factor by the total number $(2m)$ of modes, when they are assumed with equal intensity [33]. Modulational instabilities then mainly follow from the predominance of Kerr terms over SBS.

We now evaluate the growth rate of transverse modulations acting on both pump and Stokes waves assuming "perturbative" actions of the SBS nonlinearities. For the sake of simplicity, we limit our analysis to static perturbations $(\omega = 0)$ growing along the z axis only. As is well known [28,29], the maximum growth rate of transverse $[(x,y)]$ perturbations acting against a single plane-wave pump is given by $\gamma_1 = (n_2\omega_0/c) I_{1,S}$ where $I_{1,S}$ is the steady-state pump intensity. The spatial growth rate in the presence of a second counterpropagating wave can be readily evaluated. For this purpose, perturbed solutions of Eqs. (7) and (8) are first searched in the limit $g_0 \to 0$ under the form $U_i(z,t,\vec{r}_\perp) = \phi_i e^{i\lambda_i z}[1 + \varepsilon(u_i + i v_i)]$ $(i = 1,2)$, where ϕ_i, u_i, and v_i are real functions, $\varepsilon \ll 1$ and $\lambda_i = (n_2\omega_0/c)(I_{i,S} + 2I_{j,S})$ $(j \neq i)$, with $I_{1,S}$ and $I_{2,S}$ being the steady-state plane-wave intensities. Introducing the reflectivity $R_S = I_{2,S}/I_{1,S}$, the maximum growth rate can then be expressed as [36]

$$\gamma_{\max} = \frac{\gamma_1}{2}[(1 + R_S) + \sqrt{(1 - R_S)^2 + 16R_S}]. \tag{27}$$

When pump and Stokes waves have comparable intensities, $\gamma_{\max}$ can reach values three times higher than for the single pump alone. The presence of a backscattered wave thus tends to significantly increase modulational instabilities of both coupled waves.

The additional coupling to the acoustic wave via g_0 alters the former result to some extent. We suppose that modulational instability preferentially occurs at z distances where the pump depletion has almost ceased, so that I_1 and I_2 keep nearly constant value near the instability regions. To include the Brillouin gain, we consider acoustic perturbations such as $Q = Q_S[1 + \epsilon(\delta q_r + i\delta q_i)]$ with the real-valued phonon modes δq_r and δq_i and the steady-state solution $Q_S = \phi_1\phi_2^* e^{i(\lambda_1 - \lambda_2)z}$. All perturbations are assumed to exhibit an oscillatory behavior $\sim\cos(\vec{k}_\perp \cdot \vec{r}_\perp)$ in the transverse plane. By linearizing Eqs. (7)–(9), the spectral problem associated with stationary perturbative modes is found to reduce to the matrix equation

$$d_z^2 \begin{pmatrix} u_1 \\ u_2 \end{pmatrix} = \begin{pmatrix} M_{11} & M_{12} \\ M_{21} & M_{22} \end{pmatrix} \begin{pmatrix} u_1 \\ u_2 \end{pmatrix}, \tag{28}$$

with

$$M_{11} = \frac{k_\perp^2}{2k_0}\left(\frac{2n_2\omega_0}{c} I_{1,S} - \frac{k_\perp^2}{2k_0}\right),$$
$$M_{12} = \frac{k_\perp^2}{2k_0}\left(\frac{4n_2\omega_0}{c} - g_0\right) I_{2,S},$$
$$M_{21} = \frac{k_\perp^2}{2k_0}\left(\frac{4n_2\omega_0}{c} + g_0\right) I_{1,S},$$
$$M_{22} = \frac{k_\perp^2}{2k_0}\left(\frac{2n_2\omega_0}{c} I_{2,S} - \frac{k_\perp^2}{2k_0}\right).$$

The eigenvalues of Eq. (28) determine the exponential growth rate of the perturbation modes, i.e.,

$$\gamma_\pm^2 = \left(\frac{k_\perp^2}{2k_0}\right)\left[2\Delta_\pm - \frac{k_\perp^2}{2k_0}\right], \tag{29}$$

where

$$2\Delta_\pm = \gamma_1[(1 + R_S) \pm \sqrt{(1 - R_S)^2 + R_S(16 - \beta^2)}], \tag{30}$$

with $\beta = g_0 c/n_2\omega_0$. We immediately see that whenever g_0 gets close to $4n_2\omega_0/c$, the growth rate strongly decreases compared with Eq. (27). Reversely, if $g_0 \to 0$, corresponding to suppressed SBS through phase modulations, then perturbative modes grow much more rapidly along the optical path.

Figures 6(a) and 6(b) show such growth rates as a function of the transverse wave number for different values of the Brillouin gain $(\propto \beta)$. If the Brillouin gain becomes large and $\beta \to 4$ [Fig. 6(a)], the growth rate is noticeably reduced compared to a smaller Brillouin gain [Fig. 6(b)] for nonzero reflectivity. Thus, since the Brillouin gain is actually weakened for a phase-modulated pulse, modulational instabilities can be amplified by the backscattered wave, even if the latter is weak. This leads to the spatial breakup of both forward and backward waves. Note that the previous analysis was performed for static perturbations. Amplified by the rapid temporal fluctuations owing to phase modulations, time-dependent modes can be expected to lower the static instability thresholds and further increase spatiotemporal instability [36].

In the case of an amplitude modulation, the limits $g_0 \to 0$ and thereby $U_2 \to 0$ must be considered only, as the excitation of acoustic waves is aborted. This situation corresponds to the standard Bespalov-Talanov result [28] for one wave, which is known to be applicable for powerful Gaussian beams [30,31].

Initially applied to infinite media, the previous analysis should be revisited for a finite thickness of the sample $L < +\infty$. With boundary conditions, e.g., $u_1(0) = v_1(0) = u_2(L) = v_2(L) = 0$, the eigenvalues of the spectral problem must now satisfy the relationship [36]

$$\left(\frac{k_+}{k_-} + \frac{k_-}{k_+}\right)\sin(k_+L)\sin(k_-L) + 2\cos(k_+L)\cos(k_-L) - \left(\frac{\alpha_-}{\alpha_+} + \frac{\alpha_+}{\alpha_-}\right) = 0, \tag{31}$$

where $k_\pm^2 = -\gamma_\pm^2$ and

$$\alpha_\pm = \frac{k_\perp^2}{k_0}(\gamma_1 - \Delta_\pm). \tag{32}$$

Equation (31) has been solved numerically for different values of the reflectivity R_S. Its nontrivial solutions, consistent with the previous boundary conditions, yield the (static) instability threshold for the forward wave. Figure 6(c) shows the normalized threshold intensity $\gamma_1 L$ versus the normalized transverse wave numbers satisfying this equation for $R_S = 10^{-3}$. The instability threshold for $g_0 = 0.7$ cm/GW is slightly lower than the one for $g_0 = 0$. This again confirms that, even for low reflectivity, a reduced Brillouin gain, e.g., when a phase modulation is applied, can increase transverse modulational instabilities.

To check this expectation, we performed numerical simulations with an unmodulated incident pulse subject to an

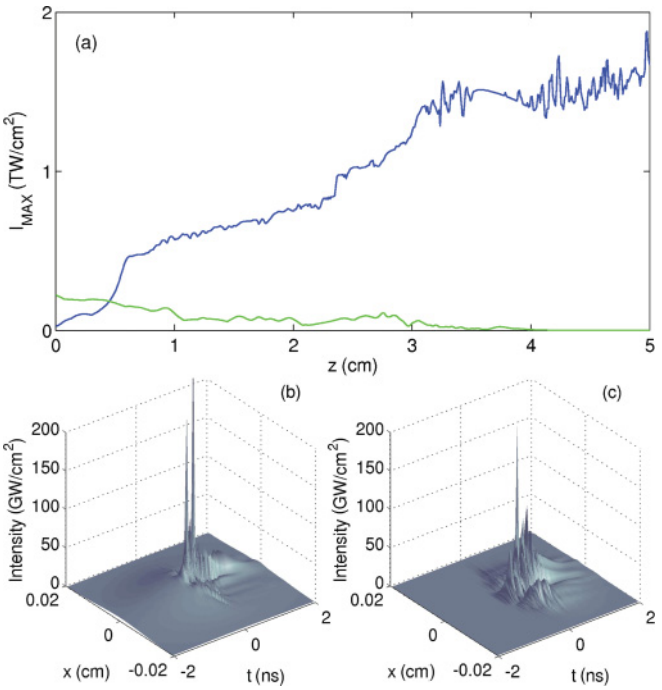

FIG. 7. (Color online) (a) Maximum intensity along the propagation axis of the pump [blue (dark gray) curve] and the Stokes wave [green (light gray) curve] for an input power $P_1(0) = 27P_{cr}$ with no phase modulation, but with an artificially reduced Brillouin gain $g_0 = 4.5/\sqrt{2m} \approx 0.7$ cm/GW. Panels (b) and (c) detail the peak intensity profiles in the (x,t) plane of the pump wave near collapse and the Stokes wave at the entrance of the sample, respectively.

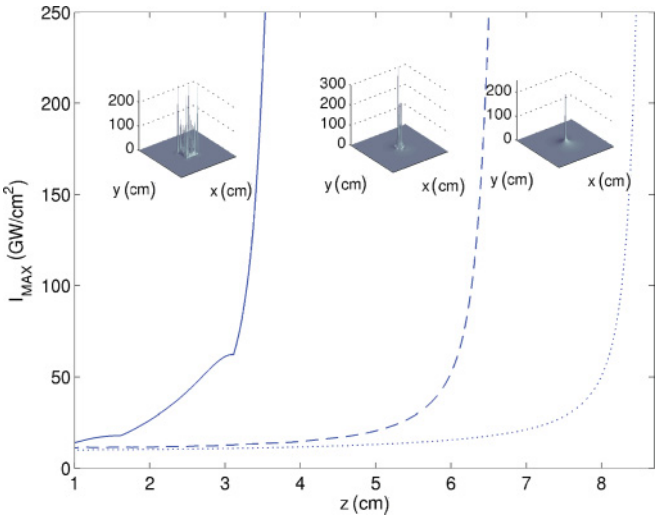

FIG. 8. (Color online) Peak intensities vs z for Gaussian and supergaussian input pulses with $I_1(0) = 10$ GW/cm^2 and $P_1(0) = 50P_{cr}$ discarding SBS. The dotted curve (right surface plot) corresponds to a pure Gaussian collapse at $z_c = 8.6$ cm, which agrees with Marburger's Eq. (14). The dashed curve (middle surface plot) represents a Gaussian input pulse with 5% amplitude random noise. The self-focusing distance is reduced to $z_c = 6.6$ cm. The solid line (left surface plot) shows the peak intensity reached by a tenth-order supergaussian pulse, collapsing at $z_c = 3.6$ cm. Insets detail maximum intensity profiles of the pump near their respective SF distances.

artificially decreased Brillouin gain. Figure 7 depicts the results for $P_1(0) = 27P_{cr}$ with a Brillouin gain of $g_0 = 4.5/\sqrt{2m} \approx 0.7$ cm/GW, i.e., an effective nonstationary gain $\sim 1/\sqrt{L_B}$ with an input laser intensity equally distributed over $2m$ modes. In Fig. 7(a), the self-focusing distance of the pump wave becomes close to that reached by the phase-modulated pump in Fig. 2(b). The peak intensity profiles in the (x,t) plane [Figs. 7(b) and 7(c)] show that both pump and Stokes beams are perturbed in time and space, similarly to Fig. 3(h). Thus, instabilities seen for phase-modulated pumps are due to the low Brillouin gain, rendering the Kerr effect dominant. The latter first amplifies temporal perturbations and, through nonlinear couplings, can also amplify spatial perturbations, especially at high input intensities.

B. Multiple filamentation

Besides from phase fluctuations, multiple filamentation can be triggered very efficiently from a random noise acting on the spatial distribution of the pump beam. To examine this aspect, we use input pulses with intensities between 5 and 10 GW/cm^2, but with higher powers, i.e., $P_1(0) = 25$–$50P_{cr}$ by increasing the beam waist up to $w_0 = 334$ μm. Without SBS, typical results are shown in Fig. 8. Without noise, the self-focusing distance is given by Marburger's formula when a Gaussian beam undergoes single filamentation. When the same pulse is perturbed by 5% random noise in amplitude, multiple filaments emerge and the self-focusing distance is shortened. For an unperturbed 10th-order supergaussian beam, the self-focusing distance is even more reduced. Seeded by the ambient (weak) numerical noise, the spatial profile forms multiple peaks on the edges of the beam, which then becomes highly turbulent.

Let us now add SBS for the same Gaussian input beam and recompute the spatiotemporal evolution for two characteristic glass thicknesses, $L = 5$ cm and $L = 10$ cm. As before, a 5% amplitude random noise is applied. First, SBS efficiency is expected to increase with the propagation length. Indeed, we can see in Fig. 9(a) that the longer the propagation distance, the more depleted the pump pulse and the more amplified the Stokes wave (see inset). Unlike in Fig. 8 discarding SBS, we do not observe severe spatial breakup [Figs. 9(b) and 9(c)], as the pump stays at moderate intensity in both cases. This is due to the action of pump depletion and of a longer diffraction length (larger beam waist), which both remotely shift the self-focusing distance according to Marburger's formula Eq. (14). Insets of Figs. 9(b) and 9(c) show Stokes intensity profiles at the entrance of the silica sample. These Stokes profiles reach a few GW/cm^2 in intensity, but they appear spatially more turbulent. This points out the high sensitivity of the Stokes waves to residual distortions of the pump induced by, e.g., remanent modulational instabilities.

Several phase modulations were then applied to the same Gaussian pump $[P_1(0) = 50\ P_{cr}]$ propagating through 10 cm of glass. With input beam intensities as low as 10 GW/cm^2, the critical bandwidth $\Delta\nu_{cr}$ becomes rather moderate, i.e., $\nu_{cr} = 336$ GHz [see Fig. 4(b)]. In this configuration, Fig. 10 reveals an interesting behavior, when using the reference

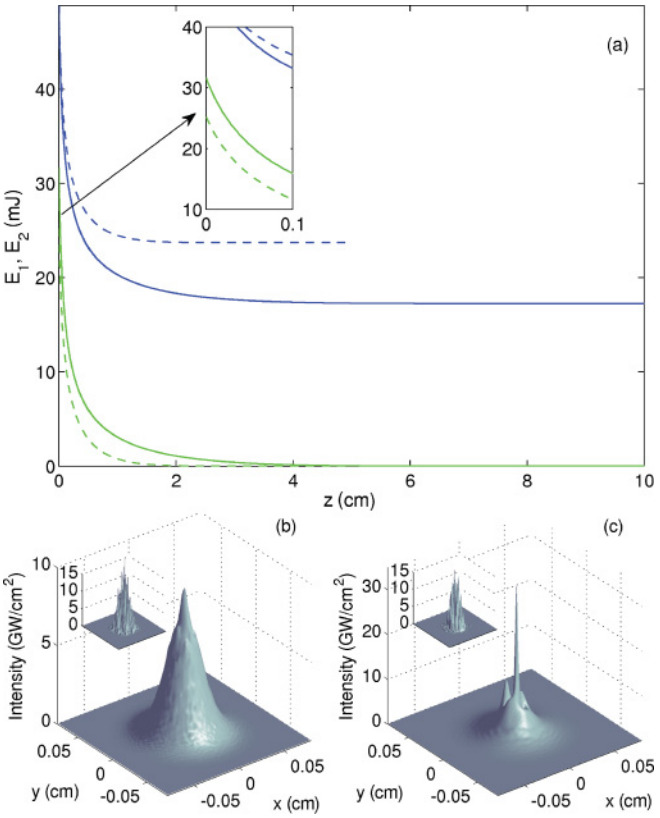

FIG. 9. (Color online) (a) Partial energies of the pump [blue (dark gray) curve] and Stokes wave [green (light gray) curve] for a 5-cm-long sample (dashed curve) and a 10-cm-long sample (solid curve). The inset details the energy levels of the Stokes waves near the entrance of the sample. Beam profiles of the pump in the (x,y) plane with maximum intensity near their self-focusing distance for power $P_1(0) = 50P_{cr}$ through (b) 5 cm and (c) 10 cm of silica. Insets show the Stokes intensity profiles at $z = 0$.

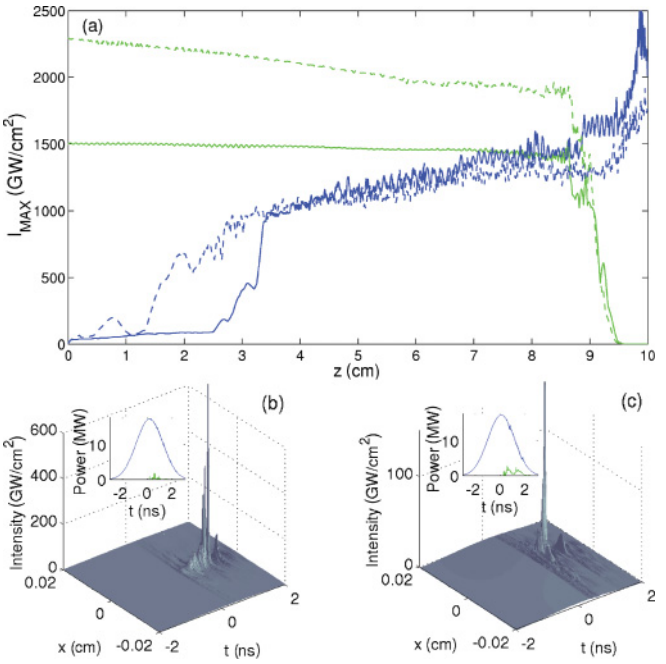

FIG. 10. (Color online) (a) Peak intensities of the pump [blue (dark gray) solid curve] and Stokes wave [green (light gray) solid curve] for a Gaussian phase-modulated pump pulse with $\Delta\nu = 84$ GHz ($\Delta\nu_{cr} = 336$ GHz) for $P_1(0) = 50P_{cr}$ along a 10-cm-long sample. Dashed curves with same color coding show the same quantities when $\Delta\nu = 42$ GHz. Pump profile in the (x,t) plane with maximum intensity near the self-focusing distance (b) with $\Delta\nu = 84$ GHz ($z_c \simeq 3.3$ cm) and (c) with $\Delta\nu = 42$ GHz ($z_c \simeq 1.6$ cm). Insets show pump [blue (dark gray) curve] and Stokes [green (light gray) curve] powers at the same distance.

bandwidth $\Delta\nu = 84$ GHz $< \Delta\nu_{cr}$. Here, the peak intensities of the pump and Stokes waves quickly reach several hundreds of GW/cm^2 [Fig. 10(a), solid curves], which departs from the dynamics shown in Fig. 9 and signals the emergence of instabilities in the pump wave. Moreover, as expected, the phase modulation significantly weakens the Stokes power [see inset in Fig. 10(b)], so that pump depletion almost vanishes. The nonlinear focus $z_c \simeq 3.3$ cm lies in between the estimate Eq. (26) [$L_{SF} \simeq 1.6$ cm] and Marburger distance [$L_M \simeq 8.6$ cm]. Surprisingly, in contrast to all previous cases, the sharp instabilities in the pump pulse responsible for this shift of the nonlinear focus are purely temporal; i.e., no transverse spatial instability takes place [see Fig. 10(b)]. It thus appears that there exists a transient regime for modulation bandwidths smaller than $\Delta\nu_{cr}$, where temporal instabilities dominate the propagation dynamics. This finding immediately raises two questions: Why do spatial instabilities not occur, and then what is the mechanism responsible for the enhanced self-focusing?

The absence of spatial instabilities is attributed to the laser input parameters. Indeed, the present pulse has an initial intensity $I_1(0) = 10$ GW/cm^2 and waist $w_0 = 334\,\mu$m, yielding $\gamma_1 \simeq 0.64$ cm^{-1} and typical transverse wave number $k_\perp = 2\pi/w_0 \simeq 118$ cm^{-1}. In contrast, the pulse presented in, e.g., Fig. 7 [$P_1(0) = 27P_{cr}$] involves a higher input intensity $I_1(0) = 27$ GW/cm^2 with $w_0 = 150\,\mu$m, which leads to larger $\gamma_1 = 1.72$ cm^{-1} and $k_\perp = 418$ cm^{-1}. In terms of MI theory [Fig. 6(b), weak Brillouin gain], the growth rate at $k_\perp$ for the low intensity case is found smaller by a factor $\leqslant 0.2$, which can justify the absence of transverse spatial instabilities. The same conclusion holds when we consider finite sample thickness [Fig. 6(c) plotted for weak reflectivity]: On the one hand, the beam developing no transverse instability [Fig. 10(b)] has a small normalized transverse wave number ($k_\perp^2 L/2k_0 \simeq 0.13$) yielding no instability intensity threshold. On the other hand, the beam with lower power suffering spatial instabilities [Fig. 7] has a higher wave number ($k_\perp^2 L/2k_0 \simeq 1.67$), for which an instability threshold exists.

The mechanism behind the enhanced pump self-focusing is that some time slices belonging to the rear part of the pump pulse and conveying power far above the SF threshold remain coupled to intense, residual Stokes time slices. We believe that this coupling keeps cross-phase modulation active and shortens the self-focusing distance expected for the pump alone.

To conclude, we made a final test by reducing the spectral bandwidth to $\Delta\nu = 42$ GHz, as an effective larger Brillouin gain should restore spatial instabilities. Figure 10(c) confirms these expectations, since turbulent patterns amplifying not only temporal but also spatial instabilities are visible. Moreover, the

pump nonlinear focus takes place near the multifilamentation distance Eq. (26), $z_c \simeq 1.7$ cm, as expected. The Stokes power and reflectivity factor are both higher, which makes the occurrence of spatial instabilities compatible with the theoretical curves of Fig. 6(b). Reflected Stokes fluences, although below the damage threshold, remain of comparable magnitude, $F_2(0) \simeq 4\ \mathrm{J/cm^2}$.

In summary, all beam configurations leading to both temporal *and* spatial modulational instabilities, involving or not phase modulations, were observed to produce a self-focusing point at the distance $z_c \approx L_{\mathrm{SF}} E_1(0)/E_1(L)$ [see Eq. (26)], within a relative margin that does not exceed 15%. A significant example is given in Figs. 2(b) and 2(e) with $P_1(0) = 27 P_{\mathrm{cr}}$, for which $z_c \simeq 0.7$ cm. This distance is far from Marburger law [Eq. (14)] predicting $L_M = 2.5$ cm. Using the multifilamentation estimate [Eq. (15)], one finds a much closer result $L_{\mathrm{SF}} = 0.58$ cm. When pump depletion is taken into account [$E_1(0)/E_1(L) \simeq 1.18$], Eq. (26) yields even better agreement with $z_c = 0.69$ cm. Another numerical example exhibits the SF distance $z_c = 1.03$ cm for $P_1(0) = 16 P_{\mathrm{cr}}$, which is faithfully reproduced by Eq. (26), yielding $z_c = 1.0$ cm. A last example can be found in the IR domain. For an input power $P_1(0) = 9 P_{\mathrm{cr}}$, we find a self-focusing distance $z_c = 0.66$ cm, whereas Marburger formula gives $L_M = 1.6$ cm and $L_{\mathrm{SF}} = 0.6$ cm. When pump depletion is taken into account, Eq. (26) yields $z_c = 0.68$ cm.

C. Influence of the beam shape

Finally, we investigate the influence of the incident beam shape, using broad spatial distributions defined by

$$U_1(x,y,0,t) = \sqrt{I_1(0)}\, e^{-t^2/t_p^2} e^{-(x^{2n}+y^{2n})/w_0^{2n}}, \qquad (33)$$

where the $1/e^2$ duration $t_p = 2.12$ ns keeps the same value as above, w_0 is the beam waist of the incident pulse, and n is the order of the supergaussian profile. At different orders of the supergaussian, the pump intensity and power are linked by the relationship

$$I_1(0) = \frac{2^{1/n} P_1(0)}{4 w_0^2 \Gamma^2\left[1 + \frac{1}{2n}\right]}, \qquad (34)$$

where $\Gamma[x]$ is the usual Gamma function. We simulate the propagation of such pulses for $n = 2$ (Fig. 11), for $n = 10$ (Fig. 12), both with $P_1(0) = 50 P_{\mathrm{cr}}$ [$I_1(0) = 10$–$40\ \mathrm{GW/cm^2}$ and $w_0 = 137$–$334\ \mu$m for $n = 2$–10], first discarding SBS and then taking it into account for 5- and 10-cm-long samples. These figures again confirm that the more depleted the pump, the larger the self-focusing distance. Besides the four most

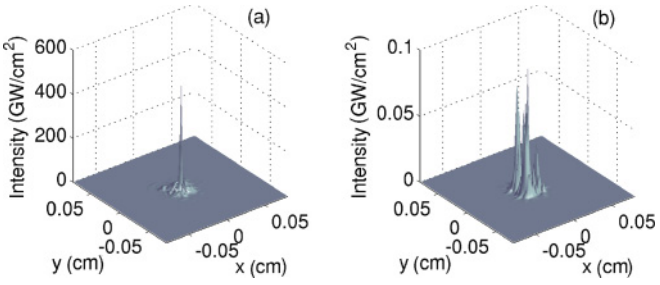

FIG. 11. (Color online) Beam profiles of the Stokes wave in the (x,y) plane with maximum intensity for a second-order supergaussian pulse ($n = 2$) and $P_1(0) = 50 P_{\mathrm{cr}}$ at the entrance of the 5-cm sample (a) for an unmodulated pump and (b) for a phase-modulated pump with $\Delta\nu \simeq \Delta\nu_{\mathrm{cr}} = 924$ GHz.

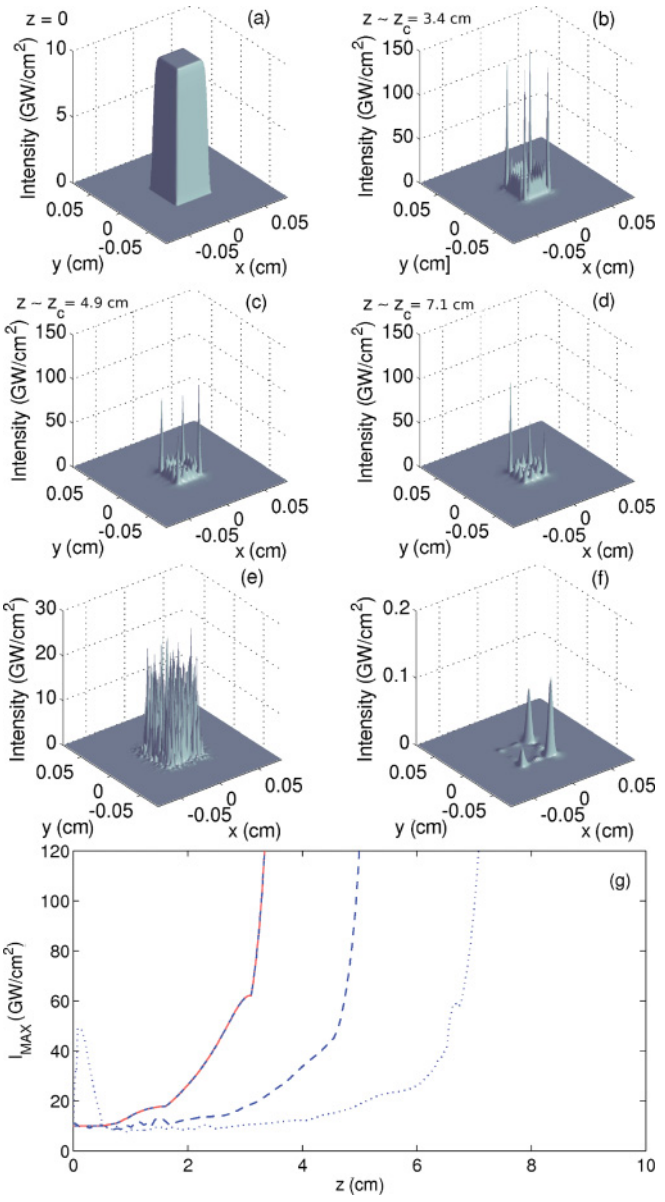

FIG. 12. (Color online) Beam profiles of the pump wave in the (x,y) plane with maximum intensity for a tenth-order supergaussian pulse ($n = 10$) and $P_1(0) = 50 P_{\mathrm{cr}}$: pump wave discarding SBS (a) at the entrance of the sample and (b) near the self-focusing distance; with SBS for (c) a 5-cm-long sample and (d) a 10-cm-long sample. Panels (e) and (f) show the Stokes profiles at the entrance of the 5-cm-long sample for an unmodulated pump and a phase-modulated pump with $\Delta\nu \simeq \Delta\nu_{\mathrm{cr}} = 636$ GHz, respectively. Panel (g) shows the peak intensities of the unmodulated pumps without SBS (solid blue curve superimposed with the dashed orange curve) and with SBS through 5 cm (dashed blue curve) and 10 cm (dotted blue curve). The dashed orange (light gray) curve corresponds to the phase-modulated pump.

intense filaments located at the apex of the amplified square patterns, the optical turbulence level inside the focal spot increases with the order of the supergaussians, while the collapse distance diminishes once multiple filamentation sets in.

Figure 11 shows the Stokes wave reflected from a second-order supergaussian pulse with $I_1(0) = 40$ GW/cm^2, $P_1(0) = 50P_{cr}$, and $w_0 = 137$ μm with (a) and without (b) phase modulation implying the spectral bandwidth $\Delta\nu = 924$ GHz ($m = 21$, $\nu_m = 22$ GHz). One observes that, even for non-Gaussian beams, broad enough spectral bandwidths sustained by a large number of modes remain efficient to suppress SBS in the SF regime. The same conclusion applies to squared beams simulated with $n = 10$, $I_1(0) = 10$ GW/cm^2, and $w_0 = 222\,\mu$m [Figs. 12(e) and 12(f)], for which backscattering is almost suppressed with a phase modulation at the critical bandwidth of $\Delta\nu_{cr} = 636$ GHz ($m = 21$, $\nu_m = 15$ GHz).

From Fig. 12, we can compare SF distances with the estimations provided by Eq. (26). For the case without SBS (b), i.e., with no pump depletion, one finds a distance $L_{SF} = 1.5$ cm, being less than half the one given by the simulation, $z_c = 3.4$ cm. This is not surprising, because in the absence of amplitude noise and SBS spatial breakup is seeded by (weak) numerical noise only. For a 5-cm-long sample including SBS (c), the depletion of the pump gives the SF distance of 5.7 cm, closer to the value of the simulation, $z_c = 4.9$ cm. Finally, for a 10-cm-long sample (d), we find a self-focusing distance $z_c = 7.1$ cm, while Eq. (26) predicts a SF distance of 9 cm. Equation (26) thus again provides a reasonably good approximation for the self-focusing distance in a multifilamentation regime involving SBS. In both cases $n = 2$ or $n = 10$, the spatial profile of the Stokes wave at the entrance of the sample, which is mainly driven by the term $\frac{g_0}{2}Q^*U_1$ of Eq. (8), is spatially perturbed and follows the "global" shape of the incident beam.

V. CONCLUSION

In summary, the competition between self-focusing and stimulated Brillouin scattering strongly depends on the characteristics of the initial pump pulse, i.e., input power, modulation, and beam shape. For low input powers, a phase modulation with moderate bandwidth $\leqslant 100$ GHz appears to be sufficient to suppress backscattering and related damages. In contrast, for higher powers [$P_1(0) > 14P_{cr}$ at $\lambda_0 = 355$ nm], phase modulations with similar characteristics (i.e., modulation depth and frequency) may still diminish the SBS pump depletion to some extent, but locally backscattered components can develop turbulent dynamics inside the material leading to nonnegligible Stokes fluences at the input facet of the sample. Phase modulations indeed tend to let the Kerr nonlinearities prevail, which forces both pump and Stokes waves to decay via modulational instabilities. In strong SF regimes, amplitude modulations with suitable ps-scaled pulse trains may be preferable to suppress backscattering. The mean energy delivered by the modulated pump will, however, be diminished by a factor close to 2.

Similar filamentation regimes can also be produced with unmodulated input pulses undergoing noisy perturbations or with supergaussian beams of sufficiently high order, promoting the breakup of the pulse's most intense edges. The self-focusing distance is always delayed by the presence of the SBS effect, because of the energy transfer from the pump to the Stokes wave. Compared with single-wave configuration, pulse breakup is reinforced in the presence of weakened SBS.

Our major result is, however, that a large enough bandwidth due to phase modulation involving a high number of modes is capable of eliminating SBS. We derive an estimate for the critical bandwidth and number of modes, which both turn out to be proportional to the input pump intensity. Applying such broadband phase modulation appears to be the most efficient strategy for suppressing SBS in high-power laser technology, since the averaged energy and power of the modulated pump should remain unaffected in that case.

ACKNOWLEDGMENTS

This work was granted access to the HPC resources of CCRT under the allocation 2010-x2010106003 made by GENCI (Grand Equipement National de Calcul Intensif).

APPENDIX A : MODEL VALIDITY VS LINEAR DISPERSION

Different terms, i.e., group-velocity dispersion and plasma coupling, have been neglected throughout the derivation of Eqs. (7)–(9). Here, these assumptions are briefly justified for $\lambda_0 = 355$ nm. The same conclusions should still hold for $\lambda_0 = 1064$ nm.

Let us first check that group-velocity dispersion (GVD) remains negligible. For this purpose, we evaluate the pump amplitude spectrum in a self-focusing regime for different types of modulation: We compute the Fourier transform of the maximum [in the (x,y) plane] pump field amplitude in the initial and self-focused states, and then we deduce its spectral width. Figure 13 shows these spectra for unmodulated, phase- and amplitude-modulated pulses at $z = 0$ (top figures) and near their nonlinear focus (bottom figures). From these, we evaluate the spectral width $\Delta\nu$ at $1/e$ and 0.05 of maximum

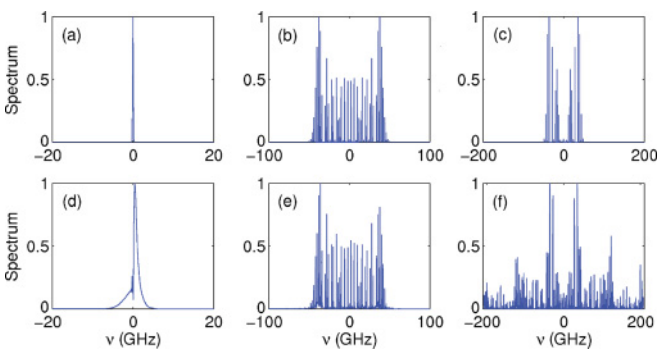

FIG. 13. (Color online) Amplitude spectra of the pump field at $z = 0$ for (a) no modulation, (b) a phase modulation, and (c) an amplitude modulation. In the self-focusing regime, at the distances (d) $z = 4.4$ cm with no modulation, (e) $z = 0.6$ cm with phase modulation, and (f) $z = 3.4$ cm with amplitude modulation ($m = 21, \nu_m = 2$ GHz).

TABLE II. Second-order dispersion term of the forward pump field near collapse for different types of modulation.

Modulation	GVD factor at $1/e$	GVD factor at 0.05
No modulation	3.6×10^{-7}	9.4×10^{-6}
Phase modulation	1.6×10^{-3}	1.9×10^{-3}
Amplitude modulation	1.4×10^{-2}	7.9×10^{-2}

amplitude and calculate the normalized GVD factor $k''\Delta\omega^2 L$, where $k'' = 1169$ fs^2/cm at 355 nm and $\Delta\omega = 2\pi\Delta\nu$ along the propagation length $L = 5$ cm. Results are summarized in Table II. In each case, the normalized GVD factor is small compared to unity, which suggests that chromatic dispersion can indeed be considered as negligible.

APPENDIX B : MODEL VALIDITY VS PLASMA GENERATION

Owing to the self-focusing dynamics, the maximum intensities of both the incident and Stokes waves can reach levels exceeding several TW/cm^2. For this reason, additional nonlinearities saturating the intensity growth, such as, e.g., plasma nonlinearities, may come into play. For modeling plasma generation, the current density term for free carriers, $\mu_0\partial_t\vec{J}$ in Eq. (2), must be evaluated. Here, the current density $J = q_e\rho v_e$ involves the density of free electrons ρ and their velocity v_e, so that $\partial_t J \approx q_e^2\rho E/m_e$, where m_e and q_e are the electron mass and charge. On the other hand, the source equation for the electron density ρ is given by the Drude model [37,38]

$$\frac{\partial\rho}{\partial t} = \rho_{\rm nt}\sigma_K I^K + \frac{\sigma}{U_i}\rho I - \frac{\rho}{\tau_R}, \tag{B1}$$

where $I = |U_1|^2 + |U_2|^2 + (U_1U_2^* e^{2ik_0z} + \text{c.c.})$ is the optical intensity, $\rho_{\rm nt} = 2.2 \times 10^{22}$ cm^{-3} is the neutral density, $\tau_R \simeq 150$ fs is the electron recombination time in silica, and $K = \text{mod}(U_i/\hbar\omega_0) + 1 = 3$ denotes the minimum number of photons necessary to extract one electron from neutral species with ionization energy $U_i = 9$ eV through a multiphoton process at 355 nm. $\sigma_K = 2.48 \times 10^{-38}$ ns^{-1} cm^6/W^3 is the associated cross section. The term $\sigma I/U_i$ corresponds to collisional ionization of free electrons with neighboring atoms and it involves the cross section $\sigma = \mu_0 q_e^2/m_e\tau_0\omega_0 k_0 \simeq 1.1 \times 10^{-19}$ cm^2, where $\tau_0 \simeq 20$ fs is the electron-ion collision time. For laser intensities limited to $\sim$10 TW/cm^2, one has $\sigma I\tau_R/U_i \ll 1$ and thus we can omit collisional ionization. Assuming a squared pulse with time extent T_0, we thus obtain

$$\rho(t) = \tau_R\rho_{\rm nt}\sigma_3 I_0^3 e^{-t/\tau_R}\left[H\left(t + \frac{T_0}{2}\right)(e^{t/\tau_R} - e^{-T_0/2\tau_R}) - H\left(t - \frac{T_0}{2}\right)(e^{t/\tau_R} - e^{T_0/2\tau_R})\right], \tag{B2}$$

where $H(x)$ is the Heaviside function. The density remains quasiconstant over typical durations $T_0 \sim 10$ ps of the highest pump peaks shown, e.g., in Fig. 3(b). Plasma losses issued from the photoionization rate $\sim W(I) = \sigma_K I^K$ are evaluated from the Poynting theorem, i.e., $J_{\rm loss}^{\rm PI} E = W(I)\rho_{\rm nt}U_i$, which leads to

$$\mu_0\frac{\partial J_{\rm loss}^{\rm PI}}{\partial t} = -ik_0\beta^{(K)} I^{K-1} E, \tag{B3}$$

where $\beta^{(K)} = \sigma_K K\hbar\omega_0\rho_{\rm nt}$ is the multiphoton absorption factor. Terms for the plasma coupling and related losses are then sorted out from Eq. (2), once plugged into ρE and $J_{\rm loss}^{\rm PI}$, respectively. Keeping only terms in $e^{ik_0z - i\omega_0 t}$ for the forward component and in $e^{-ik_0z - i\omega_0 t}$ for the backward one, one finds that Eqs. (7) and (8) must be completed by

$$-\frac{ik_0\rho_{\rm nt}\sigma^{(3)}\tau_R}{2n_0^2\rho_c}F_i U_i - \frac{\beta^{(3)}}{2}G_i U_i, \tag{B4}$$

on their right-hand side, where $F_i = I_i^3 + 4I_j^3 + 12I_i^2 I_j + 18I_i I_j^2$, $G_i = I_i^2 + 3I_j^2 + 6I_i I_j$ $(i \neq j = 1,2)$, and $\rho_c \equiv \omega_0^2 m_e\epsilon_0/q_e^2 = 8.8 \times 10^{21}$ cm^{-3} is the critical plasma density. The clamping intensity for which plasma starts to balance the Kerr terms is $I \geqslant 10.7$ TW/cm^2 for a single wave and $I \geqslant 3.2$ TW/cm^2 for the two coupled waves assumed to reach simultaneously the same saturation intensity. For intensity growth reaching only $\sim$5 TW/cm^2, plasma should thus have a limited action.

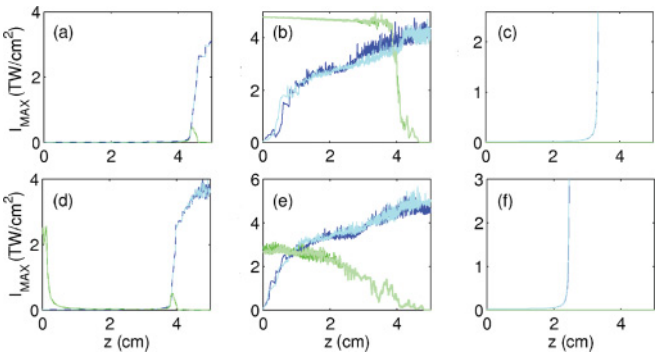

FIG. 14. (Color online) Maximum intensity along the propagation axis (a,d) without modulation, (b,e) for a phase-modulated pulse and (c,f) for an amplitude-modulated pulse with (a,b,c) $P_1(0) = 16P_{\rm cr}$ and (d,e,f) $P_1(0) = 27P_{\rm cr}$. The bright blue (green) curve shows the forward (backward) wave when the plasma response is ignored. The dark blue (green) curve shows the forward (backward) wave in the presence of plasma defocusing. In panels (a) and (d), dark and bright curves are superimposed.

Figure 14 displays evidence of the previous expectation by showing the maximum pump and Stokes intensities along the propagation axis for the pulses discussed in Fig. 2. The brighter curves refer to numerical integrations of the complete system including plasma terms, whereas the darker ones refer to the initial model equations. All dynamical behaviors remain quite similar, despite slight differences in the values of the maximal intensities when I_1 and/or I_2 reach their highest levels. This confirms the small action induced by plasma generation on the nonlinear propagation of the two optical components. We checked that accessing higher intensity levels by refining the numerical resolution did not change substantially the pulse dynamics and preserved the location of the SF distances of the pump pulse along the optical path.

[1] E. P. Ippen and R. H. Stolen, Appl. Phys. Lett. **21**, 539 (1972).
[2] V. I. Kovalev and R. G. Harrison, Phys. Lett. A **374**, 2297 (2010).
[3] H. Bercegol, L. Lamaignère, V. Cavaro, and M. Loiseau, Proc. SPIE **5991**, 59911Z (2005).
[4] J. R. Murray, J. R. Smith, R. B. Ehrlich, D. T. Kyrazis, C. E. Thompson, T. L. Weiland, and R. B. Wilcox, J. Opt. Soc. Am. B **6**, 2402 (1989).
[5] L. Lancia *et al.*, Phys. Rev. Lett. **104**, 025001 (2010).
[6] W. Han, W. Q. Huang, K. Y. Li, F. Wang, B. Feng, H. T. Jia, F. Q. Li, Y. Xiang, F. Jing, and W. G. Zheng, Chin. Phys. Lett. **27**, 124205 (2010).
[7] Y. Okawachi, M. S. Bigelow, J. E. Sharping, Z. Zhu, A. Schweinsberg, D. J. Gauthier, R. W. Boyd, and A. L. Gaeta, Phys. Rev. Lett. **94**, 153902 (2005).
[8] L. Ren and Y. Tomita, J. Opt. Soc. Am. B **26**, 1281 (2009).
[9] V. I. Kovalev, N. E. Kotova, and R. G. Harrison, Opt. Express **17**, 2826 (2009).
[10] Z. Zhu, D. J. Gauthier, and R. W. Boyd, Science **318**, 1748 (2007).
[11] G. S. He, C. Lu, Q. Zheng, P. N. Prasad, P. Zerom, R. W. Boyd, and M. Samoc, Phys. Rev. A **71**, 063810 (2005).
[12] R. W. Boyd, Editor, *Nonlinear Optics* (Academic Press, San Diego, 1992).
[13] G. P. Agrawal, *Nonlinear Fiber Optics*, 3rd ed. (Academic Press, San Diego, 2001).
[14] Y. E. D'yakov, ZhETF Pis. Red. **11**, 362 (1970) [JETP Lett. **11**, 243 (1970)].
[15] R. L. Carman, F. Shimizu, C. S. Wang, and N. Bloembergen, Phys. Rev. A **2**, 60 (1970).
[16] I. Bar-Joseph, A. A. Friesem, E. Lichtman, and R. G. Waarts, J. Opt. Soc. Am. B **2**, 1606 (1985).
[17] R. W. Boyd, K. Rzazewski, and P. Narum, Phys. Rev. A **42**, 5514 (1990).
[18] G. Arisholm and P. Narum, IEEE J. Quantum Electron. **28**, 2075 (1992).
[19] G. C. Valley, IEEE J. Quantum Electron. **22**, 704 (1986).
[20] P. Narum, M. D. Skeldon, and R. W. Boyd, IEEE J. Quantum Electron. **22**, 2161 (1986).
[21] H. Li and K. Ogusu, Jpn. J. Appl. Phys. **38**, 6309 (1999).
[22] J. M. Sajer, Proc. SPIE **5273**, 129 (2004).
[23] L. Bergé, Phys. Rep. **303**, 259 (1998).
[24] R. A. Negres, M. A. Norton, D. A. Cross, and C. W. Carr, Opt. Express **18**, 19966 (2010).
[25] S. Mauger, L. Bergé, and S. Skupin, New J. Phys. **12**, 103049 (2010).
[26] L. Bergé, Phys. Rev. E **58**, 6606 (1998).
[27] J. H. Marburger, Prog. Quantum Electron. **4**, 35 (1975).
[28] V. I. Bespalov and V. I. Talanov, ZhETF Pis'ma **3**, 471 (1966) [JETP Lett. **3**, 307 (1966)].
[29] A. J. Campillo, S. L. Shapiro, and B. R. Suydam, Appl. Phys. Lett. **23**, 628 (1973).
[30] G. Fibich, S. Eisenmann, B. Ilan, Y. Erlich, M. Fraenkel, Z. Henis, A. L. Gaeta, and A. Zigler, Opt. Express **13**, 5897 (2005).
[31] L. Bergé, C. Gouédard, J. Schjødt-Eriksen, and H. Ward, Physica D **176**, 181 (2003).
[32] E. Lichtman, A. A. Firsem, R. G. Waarts, and H. H. Yaffe, J. Opt. Soc. Am. B **4**, 1397 (1987).
[33] Y. Aoki and K. Tajima, J. Opt. Soc. Am. B **5**, 358 (1988).
[34] S. Le Floch and P. Cambon, J. Opt. Soc. Am. A **20**, 1132 (2003).
[35] H. A. Al Asadi, M. H. Al Mansoori, S. Hitam, M. I. Saripan, and M. A. Mahdi, Opt. Express **19**, 1842 (2011).
[36] G. G. Luther and C. J. McKinstrie, J. Opt. Soc. Am. B **7**, 1125 (1990).
[37] S. Skupin and L. Bergé, Physica D **220**, 14 (2006).
[38] L. Bergé, S. Skupin, R. Nuter, J. Kasparian, and J. P. Wolf, Rep. Prog. Phys. **70**, 1633 (2007).